Automated Recovery of the Center of Rotation in Optical Projection Tomography in the Presence of Scattering

Di Dong, Shouping Zhu, Chenghu Qin, Varsha Kumar, Jens V. Stein, Stephan Oehler, Charalambos Savakis, Jie Tian, *Fellow, IEEE*, and Jorge Ripoll

***Abstract*—Finding the center of rotation is an essential step for accurate 3-D reconstruction in optical projection tomography. Unfortunately, current methods are not convenient since they require either prior scanning of a reference phantom, small structures of high intensity existing in the specimen, or active participation during the centering procedure. To solve these problems this paper proposes a fast and automatic center of rotation search method making use of parallel programming in graphics processing units. Our method is based on a two step search approach making use only of those sections of the image with high signal-to-noise ratio. We have tested this method both in nonscattering *ex vivo* samples and in *in vivo* specimens with a considerable contribution of scattering such as *Drosophila melanogaster* pupae, recovering in all cases the center of rotation with a precision 1/4 pixel or less.**

***Index Terms*—Center of rotation, optical projection tomography (OPT), parallel reconstruction, scattering.**

I. Introduction

OPTICAL projection tomography (OPT) is a high-resolution 3-D imaging technique whose sample size is usually between 1 and 10 mm [1]–[3], depending on the amount of scattering present. Originally applied only to *ex vivo* samples [1], the current applications of OPT also deal with *in vivo* samples with a significant amount of scattering. OPT can be applied either in a transmission or an emission mode [4], the first based on recording absorption changes while the second relies on recording fluorescence emission [5]–[7]. OPT is an effective imaging tool for either cleared samples or low scattering biological specimens [8]–[13]. In this study, we have chosen to implement our methodology in two instances in order to cover all possibilities that OPT offers: *in vivo* OPT of a developing *Drosophila melanogaster* pupa (scattering sample) and the more established *ex vivo* OPT on a fixed and cleared lymphnode (nonscattering sample).

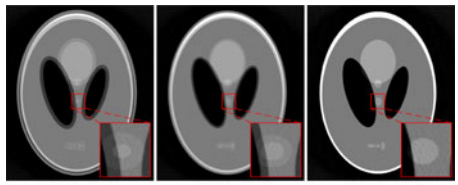

Fig. 1. Effect of rotational center offset in reconstructed images. The unit of the offset is the detector pixel number.

Once the OPT data are collected, several methods can be used to reconstruct the 3-D volume from projection views such as the filtered back-projection (FBP) [14], [15] and weighted filtered back-projection methods [16], among others. These methods convert the projection views to sinograms and then reconstruct the 3-D volume slice by slice, being a sinogram the angular sequence of a row in the projection views which corresponds to a horizontal slice in the 3-D volume. However, the problem of a center of rotation displaced from the center of the image used for reconstruction is a common occurrence in OPT experiments and such a center offset will considerably blur the images even if it is of only a few pixels (see Fig. 1 for an example). It is therefore essential for high-quality reconstructions to find the true center position and account for it during reconstruction.

Since precise calibration of the OPT setup prior to each individual scan is in most cases unfeasible (note that simply placing a new sample on the sample holder might displace the rotational center a few pixels), there are several papers discussing the calculation of the displaced center position without using prior calibration scans [14], [17], [18]. Taking [14] as an example, a method is proposed consisting of searching for the center position by reconstructing the same slice several times with different offset values, and then choosing the optimum offset value either visually or using the total variance of the reconstructed slice, which is found as the squared deviation of all pixel values. There are several disadvantages to this method, the first

Manuscript received May 6, 2012; revised August 4, 2012, and August 25, 2012; accepted September 10, 2012. Date of current version February 4, 2013. This work was supported in part by the Bill and Melinda Gates Foundation, the National Basic Research Program of China (973 Program) under Grant 2011CB707700, the Fellowship for Young International Scientists of the Chinese Academy of Sciences under Grant 2010Y2GA03, the National Natural Science Foundation of China under Grant 81101084. The work of J. Ripoll was supported under project "Minos" by the Greek National program Thalis.

D. Dong, C. Qin, and J. Tian are with the Intelligent Medical Research Center, State Key Laboratory of Management and Control for Complex Systems, Institute of Automation, Chinese Academy of Sciences, Beijing 100190, China (e-mail: dongdi@fingerpass.net.cn; qinch@fingerpass.net.cn; tian@ieee.org).

S. Zhu is with the School of Life Science and Technology, Xidian University, Xi'an, Shaanxi 710071, China (e-mail: zhushouping@life.xidian.edu.cn).

V. Kumar and J. V. Stein are with the Theodor Kocher Institute, University of Bern, Bern 3012, Switzerland (e-mail: kumarv@hss.edu; jstein@tki.unibe.ch).

S. Oehler and C. Savakis are with the B.S.R.C. Alexander Fleming, Varkiza 16602, Greece (e-mail: oehler@fleming.gr; savakis@fleming.gr).

J. Ripoll is with the Institute of Electronic Structure and Laser, Foundation for Research and Technology-Hellas (FORTH), Heraklion 71110, Greece (e–mail: jripoll@iesl.forth.gr).

Color versions of one or more of the figures in this paper are available online at http://ieeexplore.ieee.org.

Digital Object Identifier 10.1109/TITB.2012.2219588

one being that the offset search region must be given manually *a priori*. Second, the offset search region should cover the true center and be narrow enough, otherwise the method might collapse. Additionally, this process is time consuming since several slices need to be reconstructed many times. Another option is to use the sharp edges or high-intensity structures in the specimen to calculate the offset [17], [18], but such sharp features are often not available in OPT, specifically when imaging distributed fluorescence or in the presence of scattering. In [19], a semiautomatic centering method for cleared specimens has been presented through prior scanning two perpendicular images. The drawback of this method is that in the presence of scattering or out-of-focus data two perpendicular views are not enough to locate with the required precision the rotational center. Zhu *et al.* have proposed a specimen motion correction method for transmission OPT based on Helgason–Ludwig consistency condition [20], which can automatically find the rotational center. However, the motion correction method can only be utilized in transmission OPT in the absence of scattering, and thus cannot find the rotational center in emission OPT when scattering is present. Finally, a center of the mass based method has been introduced in computed tomography (CT) applications, which can automatically find the rotational center [21]. Unfortunately, its use in OPT is limited since OPT may suffer from out-of-focus problems, a feature unique to optics, which means that opposing views might differ due to the effects of the depth of field [1], or due to the inhomogeneous optical properties of the sample. Additionally, this method is sensitive to noise, which is usually present in OPT data since low intensities and short exposures are required to reduce photobleaching to a minimum. For the aforementioned reasons, the development of a fast, automatic, and robust method to calculate the rotational center in OPT is a necessity.

Additionally to an automated and robust center of the rotation estimation method, there is a significant hurdle that needs to be overcome with respect to the long computation times needed to reconstruct the large datasets typically present in OPT [22], [23]. Basu and Bresler have proved that 3-D tomography reconstruction with the commonly used back-projection method has a computational complexity of $O(MN^2\log(N))$, being M the number of projection angles and N the width in pixels of the image [24]. Although graphic processing unit (GPU)-based reconstruction methods have been proposed in OPT [25] and CT [26] to speed up the reconstruction process, there is still room for improvement of the reconstruction speed.

This paper is organized as follows: in Section II, we present an overview of our OPT experimental setup, explaining the practical implementation of both the rotational center search and fast reconstruction in Section III. Section IV includes a detailed analysis of our method and some experimental results, which include *in vivo* imaging of scattering samples and *ex vivo* results for cleared specimens. Within this section, we present a study on the relation between the specimen signal intensity (SSI) and centering errors, a comparison with other methods, and a reconstruction speed test. Finally, discussion and conclusions are covered in the last section.

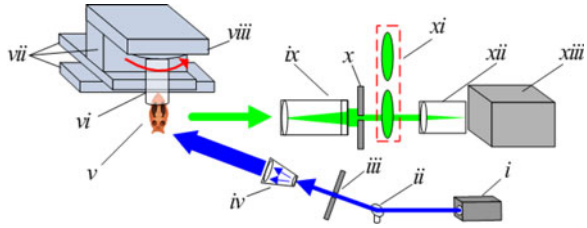

Fig. 2. OPT setup used to acquire the *in vivo* data: (i) cw laser, (ii) mirror, (iii) shutter, (iv) beam expander, (v) specimen, (vi) capillary tube, (vii) linear positioning stages, (viii) rotation stage, (ix) microscope objective, (x) variable aperture, (xi) filter wheel, (xii) tube lens, (xiii) CCD camera.

II. Experimental OPT Setup

Fig. 2 shows the OPT setup used to acquire the experimental *in vivo* data (for details on this setup, see [12], [13], [18], [27]). In general terms, a laser is guided and expanded before impinging on the sample in almost epi-illumination geometry (see Fig. 2). Care is taken to ensure the beam is as homogeneous as possible, providing a 20-mm spot size at the plane of the sample. The sample is rotated and its position controlled using three linear positioning stages. Since *in vivo* applications are in mind, the specimen is surrounded by air instead of index matching fluid. The imaging unit consists of a tube lens, a filter wheel and a microscope objective (in all results shown a 5 $\times$ was used). For the *in vivo* experiments shown herein, we used a band-pass fluorescence filter centered at 525 $\pm$ 17.5 nm and a 473 nm laser appropriate for the green fluorescent protein (GFP). Immediately behind the objective an iris is placed to control the depth of field. Finally, images were collected with an intensified CCD (iXon DV885 ANDOR Technology, Belfast, Northern Ireland) with a 1004 $\times$ 1002 chip and a 14-bit dynamic range. All experiments were controlled through a PC running on 64-bit windows 7 using custom made Labview functions (National Instruments, TX).

For the *in vivo* experiment, a *Drosophila melanogaster* early stage pupa which expresses GFP ubiquitously [28] was carefully attached to the lower tip of a capillary, securing the other end to the rotation stage. Room temperature was kept to ensure the pupa could develop normally. An OPT dataset was acquired by taking 330 projection images spanning the complete 360° using a 2 $\times$ 2 binning and slight cropping to obtain 500 $\times$ 500 sized 16-bit images.

III. Methods

In this section, we describe how the automatic search for the rotational center and fast reconstruction are implemented. We shall make use of data obtained *in vivo* from the early pupa stage and reconstruct a 500 $\times$ 500 $\times$ 500 sized volume. We will first introduce OPT imaging, then the rotational center search and finally the GPU-based reconstruction.

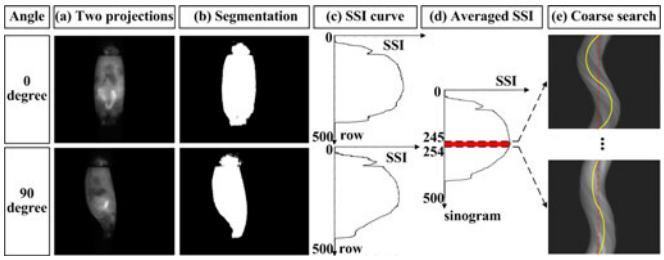

Fig. 3. Scheme of sinogram selection. (a) Choice of two perpendicular views. (b) Threshold segmentation. (c) Calculation of SSI for each row. (d) Calculation of SSI for each sinogram. (e) Coarse search on selected sinograms.

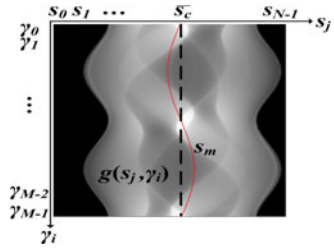

Fig. 4. Center of mass method applied to a sinogram. The red line "s_m" represents the projection of the center of mass for each angle, while $\overline{s_c}$ is the least squares estimate of the rotational center.

A. OPT Imaging

In transmission OPT in the absence of scattering light transmitted can be expressed as a 2-D Radon transform:

$$g(s,\gamma) = \iint f(x,y)\delta(x\cos\gamma + y\sin\gamma - s)dxdy \qquad (1)$$

with δ being the Dirac delta function and $g(s,\gamma)$ the projection of the function $f(x,y)$ onto the direction γ. In transmission OPT $f(x,y)$ represents the absorption coefficient of the tissue being imaged while $g(s,\gamma)$ is the measurement at a line of pixels of the CCD. When $g(s,\gamma)$ is known in (1) the process of calculating $f(x,y)$ is usually termed the inverse Radon transform (see [29], for example).

The most commonly used method for the inverse Radon transform is the FBP, which includes two steps: 1) Fourier transform and filter the 1-D projection data and 2) back-project all angles to the reconstructed slice in the spatial domain. This second step is the crucial one: if there exists a displacement with respect to the center of rotation in the OPT setup and it is not corrected prior to this step the final image will be seriously blurred. Thus, the true rotational center should be found before this second step.

B. Determining the Center of Rotation

The proposed automatic search for the center of rotation requires that 1) the detector and rotation stage are not tilted allowing only for horizontal displacement, 2) all projection views have the same center of rotation, and 3) the projection data are not truncated (all projection views fully cover the sample). Our method requires three steps, namely a sinogram selection, a coarse search, and a fine search.

1) Sinogram Selection: Not all sinograms in OPT are suitable for center search since some may contain reduced information on the specimen (see Fig. 3(a) where two views are presented; clearly, the sinograms at the two vertical ends of the projection view have no information on the specimen, and thus should be rejected). In order to automatically establish the center of rotation, we defined the SSI by assigning a weight to each sinogram, calculated as the ratio of the sample region to the whole region of the sinogram, which will be implemented only on two perpendicular views to increase speed. Sinogram selection is done automatically prior to the coarse search to establish which sinograms will be used for centering.

Fig. 3 shows the sinogram selection scheme. Since two perpendicular views are a rough estimate of the shape of the specimen [see Fig. 3(a)], we used these to calculate the SSI of all sinograms. Threshold segmentation on the two views is used to distinguish the sample from the background regions, selecting the threshold as the average value of each projection [see Fig. 3(b)]. Once segmented, the SSI of a row in the projection is calculated as the number of sample pixels inside it. The SSI curve of different rows in the projection is shown in Fig. 3(c) with the vertical axis representing the row index and the horizontal axis the SSI of the row. The SSI of each sinogram is evaluated as the average SSI of its rows in the two projections. An example of the SSI curve of different sinograms is shown in Fig. 3(d). Once this curve is found, one or several sinograms with the highest SSI can be selected for the center of rotation search. In the results shown here we selected ten sinograms with the highest SSI (shown in Fig. 3(d) between sinogram numbers 245 and 254) for both coarse search and fine search.

2) Coarse Search: The coarse position of the center of rotation is found by using the center of mass of the specimen. This approach has been previously presented to calculate the rotational center of 2-D parallel-beam CT in [21]. In parallel-beam CT geometry (and thus in the OPT setup presented here), the center of mass of the object is projected onto the center of mass of the projection as follows:

$$s_m(\gamma) = s_c + x_m\cos\gamma + y_m\sin\gamma \qquad (2)$$

where (x_m, y_m) is the object's center of mass in the spatial domain and $s_m(\gamma)$ is the projection's center of mass at angle γ. s_c is the center of rotation projected onto the detector, which should be the same for all angles in a parallel-beam geometry and represents the rotational center position we want to find. We consider M uniformly distributed measurements spanning the complete 360°, with which we obtain M discrete equations of (2). After simplifying, we can calculate the least squares estimate of s_c [21] as follows:

$$\overline{s_c} = \frac{1}{M}\sum_{i=0}^{M-1} s_m(\gamma_i) \qquad (3)$$

where the relationship of $\overline{s_c}$ and $s_m(\gamma_i)$ is shown in Fig. 4. The projection angle γ_i is denoted by

$$\gamma_i = \frac{i2\pi}{M}, \quad i = 0,\ldots,(M-1). \qquad (4)$$

The discrete center of mass on the detector at angle γ_i is

$$s_m(\gamma_i) = \frac{\sum_{j=0}^{N-1} s_j g(s_j, \gamma_i)}{\sum_{j=0}^{N-1} g(s_j, \gamma_i)} \tag{5}$$

where N is the element number of the line detector (i.e., one line of the CCD image), s_j represents the position of each element with j ranging from 0 to $N-1$, and $g(s_j, \gamma_i)$ is the detector pixel value of position (s_j, γ_i) in the sinogram.

In principle, the center of mass method could be successfully applied in a scattering-free CT and thus in ideal conditions in our OPT. However, in practice, several factors impair this technique such as mechanical movements/displacements during the experiment, noise, changes in image sharpness as parts of the object move in and out from the depth of field, and more importantly, due to the fact that opposing views might have different fluorescence images due to the optical inhomogeneity of the sample.

Although the center of mass cannot be used for precise centering in OPT, it can automatically locate, in a robust manner, the center near the true position when used combined with our high SSI sinogram selection. After selecting the high SSI sinograms, we apply (5) to establish its center of mass s_m and then (3) to calculate the sinogram's coarse center of rotation s_{coarse}. Finally, we average all positions obtained from the selected sinograms to obtain the average coarse center of rotation, $\overline{s_{\text{coarse}}}$ (note that these points also contain information on the tilt of the axis of rotation). Once we have a coarse approximation of the true center of rotation, we then improve the accuracy by performing a fine search based on the variance of the reconstructed slice.

3) Fine Search: Although the coarse search can automatically estimate the center position, the result is in practice not accurate enough. In order to improve accuracy, we therefore perform a fine search step near the averaged coarse center of rotation $\overline{s_{\text{coarse}}}$. The variance method is proven to have a location accuracy better than 1/8th of a pixel [14] if the search region covers the true center of rotation and does not span too many pixels (high variance far away from the true center does not necessarily imply a sharp reconstruction). Thus, we have limited the search region to less than 40 pixels around an initial center position using a step of 1/8 of a pixel [14].

In our fine search step, we adopt the variance method but search only on the selected high SSI sinograms in order to minimize the influence of noise, making use of the averaged coarse position $\overline{s_{\text{coarse}}}$ as the starting center of rotation. The variance of the pixel values in a reconstructed image F_{variance} is calculated as follows:

$$F_{\text{variance}} = \frac{\sum_{y=0}^{N-1} \sum_{x=0}^{N-1} (f(x,y) - \overline{f})^2}{N^2} \tag{6}$$

where $\overline{f} = \frac{\sum_{y=0}^{N-1} \sum_{x=0}^{N-1} f(x,y)}{N^2}$ is the average pixel value of the reconstructed slice. $f(x,y)$ is the pixel value of a reconstructed slice, where both x and y range from 0 to $N-1$. To increase speed, we run first a search with 1 pixel step over a 40 pixel region centered at $\overline{s_{\text{coarse}}}$ to find a better center position s'_{fine} (see Fig. 5) and then an exhaustive search with a 1/8 pixel step over a 2 pixel region to establish the center position s_{fine}, where the reconstructed image is least blurred and therefore presents the maximum variance. Finally, we average the fine centers found s_{fine} of all selected sinograms to obtain the final center of rotation $\overline{s_{\text{fine}}}$.

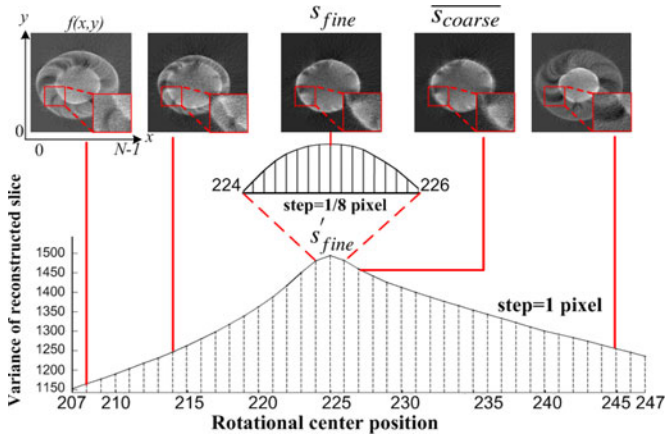

Fig. 5. Fine search with variance method and search step change. The combination of step = 1 pixel and step =1/8 pixel is used for acceleration.

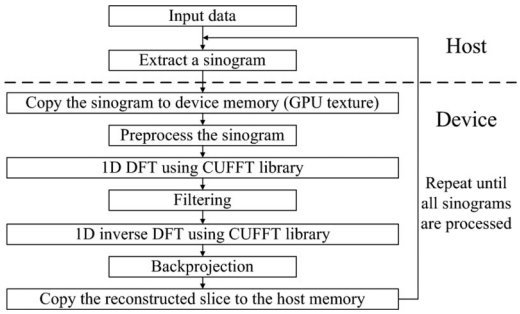

Fig. 6. Scheme of the GPU implementation of FBP method.

C. Parallel Reconstruction With Circular FOV

Since speed is fundamental when dealing with large datasets, the fine search step was done making use of GPU parallel programming, dramatically increasing the speed. The center search process was performed on a desktop computer running on 64-bit Windows 7, with an Intel Core2 2.66 GHz CPU, a 2GB DDR2 RAM, and an NVIDIA GTX 275 GPU card containing an 896 MB device memory. The fine search time of each sinogram was about 0.320 s which includes 56 reconstructions, variance calculations and maximum variance selection. In this study, the Common Unified Device Architecture (CUDA, NVIDIA corporation) was used to code the fast FBP reconstruction. Fig. 6 shows our CUDA-based FBP scheme where the sequential codes are executed on the CPU (host), while the parallel codes, such as filtering and back-projection, are executed on the GPU (device).

In order to further optimize the reconstruction speed, the geometry of the FOV is taken into account in the back-projection step since the reconstructed area is not square, but a disk whose voxels are always projected onto the detector during the whole scan. Voxels outside the circular region are directly set to zero and the back-projection step skipped. In this manner, the circular

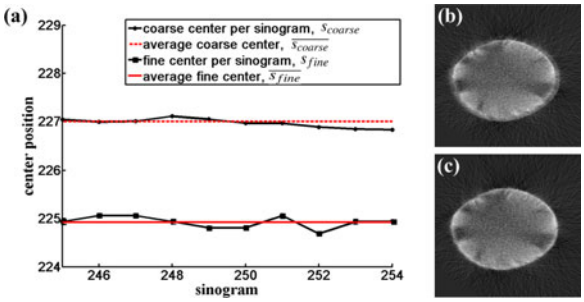

Fig. 7. Centering results for an early stage *D. melanogaster* pupa expressing GFP ubiquitously. (a) Centering results on ten selected sinograms. (b) Reconstructed slice with average coarse center. (c) Reconstructed slice with average fine center.

FOV scheme can reduce the back-projection time by at least a $\frac{\pi}{4}$ factor.

IV. Experiments and Results

In this section, we present results obtained using the automatic centering as well as a detailed analysis of our method.

A. In Vivo Experiments on Drosophila Melanogaster

Fluorescence OPT data were acquired from an early stage pupa of *D. melanogaster* using the setup described in Section II and [12], [13], [18], [27]. After scanning, both automatic center search and fast reconstruction using GPUs were applied to the data. The centering results using the ten selected sinograms with highest SSI are shown in Fig. 7. Fig. 7(a) shows the centering results where the average coarse center $\overline{s_{\text{coarse}}}$ is 2 pixels off the true rotational center (located at 225) and the average fine center $\overline{s_{\text{fine}}}$ is 0.066 pixel off the true center. Fig. 7(b) shows a slice reconstructed with $\overline{s_{\text{coarse}}}$ which is slightly blurred, underlying the fact that we might be near the true center of rotation but have not found it yet. Fig. 7(c) shows a slice reconstructed with $\overline{s_{\text{fine}}}$, which as can be seen is much sharper than with $\overline{s_{\text{coarse}}}$. Note that the accuracy is 0.066 pixel which is better than the 1/8 pixel of the variance method [14] due to the fact that we used the average position of the ten sinograms with highest SSI.

The 3-D results of the pupa are shown in Fig. 8, where we can clearly distinguish several of the anatomical features at the early development stage prior to head eversion (see Fig. 8(e) for a reference anatomical map [30]), even though these specimens present a considerable amount of scattering.

B. Analysis of SSI and Centering Errors

We have investigated the relation between centering errors and the SSI by performing coarse-fine centering using all sinograms of the *in vivo* data. The results showed that coarse-fine search on a high SSI sinogram (top 50% sinograms in SSI curve) had accuracy better than 1 pixel while the accuracy for low SSI sinograms (bottom 50% sinograms in SSI curve) could be as bad as 5 pixels, highlighting the fact that high SSI selection improves the accuracy of our method. In order to establish the robustness of our method with respect to the choice of the initial angle (note that in the previous results the SSI was calculated using initial angle 0° and its perpendicular angle 90°) we have also investigated the relation between selected sinograms and initial angle using the *in vivo* data. The results showed that even though the sinogram with highest SSI obtained could vary slightly (in the results, we analyzed it varied between 40 sinograms) we found that using the coarse-fine method invariably on the highest SSI sinogram had an accuracy better than 1/4 pixel irrespective of the initial rotational angle chosen. When selecting the ten highest SSI sinograms we found this error to decrease to less than 1/8 pixel, further demonstrating the robustness of our method.

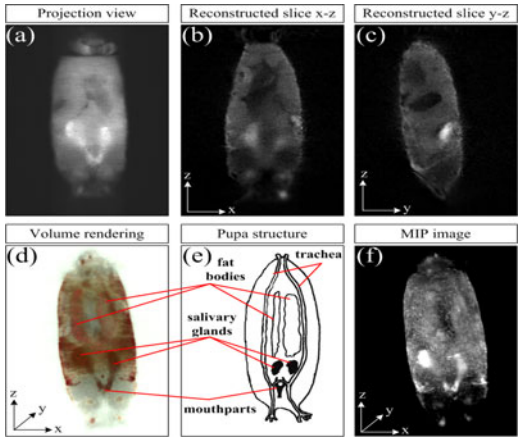

Fig. 8. Reconstruction results for early stage *D. melanogaster* pupa measured *in vivo*. (a) Projection view at 0°. (b) Reconstructed slice in the x–z plane. (c) Reconstructed slice in the y–z plane. (d) Volume rendering of the 3-D result. (e) Anatomy of the main structures in the pupa. (f) Maximum intensity projection of the reconstruction.

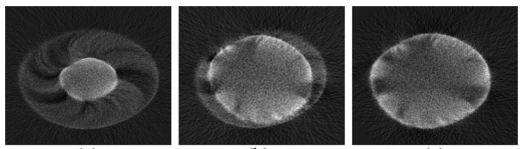

Fig. 9. Comparative experiments between [20] and our method. (a) Without correction. (b) Method in [20]. (c) Our method.

In order to compare our results with previous methods, we have done a comparative experiment between the method in [20] and our method. In [20], an automated motion correction method was proposed which converts the rotational center offset to specimen translation and corrects it by translation estimation. Fig. 9 shows the results, where (a) presents a reconstructed slice without any correction, (b) shows the slice using the translation motion correction in [20], and (c) presents the slice corrected by our coarse-fine centering. The motion correction method in [20] failed to find the correct rotational center offset since it is currently valid only for transmission OPT imaging, requires a reference image, and fails in the presence of scattering.

C. Ex Vivo Experiments on Mouse Peripheral Lymph Node

In order to make sure that our method can be applied to a variety of data, we tested it on OPT data obtained from a commercial OPT scanner (BioOptonics, U.K.). The experiment was performed on a BABB-immersed (a 1:2 mixture of

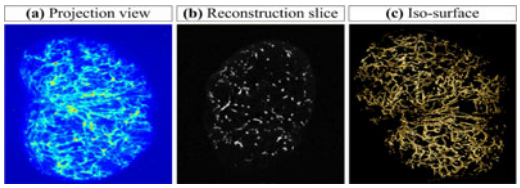

Fig. 10. Reconstruction results of a mouse PLN. (a) Projection view of the PLN as measured by the CCD. (b) Reconstructed slice. (c) Isosurface rendering of the volume.

TABLE I
RECONSTRUCTION SPEED TEST ON DIFFERENT DATASETS

Process Step	Scheme	256×256×256	512×512×512	1024×1024×1024
Back-projection on device	no Circular FOV	0.408 s	3.063 s	21.575 s
	Circular FOV	0.361 s	2.511 s	18.422 s
Total reconstruction on device	no Circular FOV	0.601 s	3.996 s	26.550 s
	Circular FOV	0.546 s	3.444 s	23.378 s

Benzyl Alcohol–Benzyl Benzoate) mouse peripheral lymph node (PLN), the goal of which was to image the high endothelial venule (HEV) networks. The filter sets, exciter 545 nm/30 nm and emitter 617 nm/75 nm, were used to acquire a fluorescent signal for a total of 500 projections. The detailed work-flow and setup of this experiment were described in [31]. Since the contribution of scattering was weak, we performed coarse-fine centering only on the highest SSI sinogram, which took 0.554 s and yielded a centering error of 0.113 pixel, once again less than 1/4 pixel. Fig. 10 illustrates the results obtained making use of our centering result, where (a) shows a raw emission image from the camera, (b) shows a reconstructed slice, and (c) shows the isosurface rendering of the volume. The results obtained show that the HEV networks were reconstructed accurately and results comparable to those shown in [31]. In this experiment, we also tested the coarse-fine centering on ten sinograms which took 5.538 s with an error of 0.085 pixel (less than 1/8 pixel).

D. Reconstruction Speed Comparison

In order to test the speed of the parallel reconstruction using GPUs, a set of simulation experiments with different data sizes were evaluated without the preprocessing and center searching steps. The reconstruction process on the device includes four steps: sinogram copy from host memory to device memory, filtering on the device, back-projection on the device, and transfer of the result from the device memory to the host memory. The processing time of back-projection and total reconstruction with and without the circular FOV are shown in Table I. With regard to the back-projection time on the GPU, the circular FOV method was faster than traditional methods. The back-projection time cost ratios between circular FOV and normal methods were $\frac{0.361}{0.408} = 88.5\%$ for volume $256 \times 256 \times 256$ in size, $\frac{2.511}{3.063} = 82.0\%$ for a volume $512 \times 512 \times 512$ in size and $\frac{18.422}{21.575} = 85.4\%$ for a $1024 \times 1024 \times 1024$ sized volume. These ratios were close to the theoretical value of $\frac{\pi}{4} = 78.5\%$.

Here, we also compared the reconstruction speed with [25], which was also GPU-based OPT reconstruction with an NVIDIA GPU card (Tesla C1060, 240 streaming processors, 4Gbyte memory) and a CPU (Intel Core at 3.16 GHz with 3 GB RAM). The projection data were $512 \times 512 \times 360$ in size and the reconstruction volume was $512 \times 512 \times 512$ in size, which is the same as in [25]. The authors presented results with 3.8 s reconstruction time for the volume without data transfer time between host and disk, while ours was 3.444 s, underlying the advantage of using the circular FOV method.

V. DISCUSSION AND CONCLUSION

This paper proposes a fast and automated method to locate the rotational center in OPT, and as well as a fast implementation for the reconstruction. The relevant points of this paper can be summarized as follows. First, our coarse-fine centering method can automatically locate the center of rotation without prior scanning or direct participation. Although prior scanning of a phantom such as a cylindrical rod can be used in a calibration experiment to find the center of rotation instead of a center search algorithm, the system geometry often changes in those setups where different sized samples (or different objectives) are used and frequent centering prior to scanning is time consuming and prone to error. On the other hand, the semiautomatic positioning method [19] and the variance-based exhaustive search methods [14], [18] require direct interaction. Comparing to these approaches, our method locates the center of rotation automatically making use of only the projection views, rendering it straightforward, general and easy to implement.

Second, the high SSI sinogram selection step and coarse-fine search makes our centering method robust and precise. The SSI is introduced in this paper to identify those high-quality sinograms which will give the optimum centering accuracy. Our experimental results show that centering on a high SSI sinogram is more likely to find the true center of rotation. Comparing to other highly precise center of rotation search methods, such as the least squared fitting of highly structured point-like region of a sinogram [18] and sharp edge-based centering [17], high SSI sinogram selection can be applied to more generic samples where these sharp edges or highly structured points might not be available (as in the *D. melanogaster* pupa presented in this study). Both *in vivo* and *ex vivo* experiments show that coarse-fine search on ten sinograms yields a centering error of less than 1/8 pixel.

Finally, our centering method is very fast. The search step change scheme can reduce 82.5% reconstruction load during fine search (in the cases presented here from 320 reconstructions to 56 reconstructions). Meanwhile, the parallel reconstruction with circular FOV can boost additionally the reconstruction speed on the GPUs by more than 10% when compared to [25]. Both the *in vivo* (scattering) and *ex vivo* (nonscattering) experiments illustrate that a coarse-fine search only on the highest SSI sinogram takes less than 0.6 s and gives an accuracy better than 1/4 pixel. If we perform the same search on a sinogram with a variance-based exhaustive search method [14], the time is more than 60 s without aforementioned acceleration schemes. It is clear that fast reconstruction is a necessity when large amounts of OPT data need to be reconstructed (as in time-lapse *in vivo* imaging, for example). Additionally, fast reconstructions can offer real-time feedback during the experiment as shown

in [25], dramatically shortening the experiment's operation time, which ensures a high survival rate of the sample and low photobleaching.

In this paper, we have shown results in the presence of a significant contribution of scattering, and have applied the method for imaging *D. melanogaster* pupae *in vivo*. We have shown that good quality images can be obtained in a fast and robust manner. However, we believe that there is still room for improvement: accounting for scattering in the reconstructions will be the next step, at least in those cases where light propagation has not lost all its original direction (i.e., when the diffusive contribution is still not dominating). During the fine step of our method the image variance within slices is used as a figure-of-merit (FOM) to quantify image quality. Besides the image variance, other effective FOMs developed originally for CT can also be applied to our method. In [32], for example, the image entropy is used as the FOM during misalignment correction for circular cone-beam CT. In addition, the image normalized sharpness is utilized as the FOM during the automatic alignment of tomographic projection data in [33]. These FOMs are effective and can also be applied to our fine step search approach. Meanwhile, further improvement of the center search method in order to account for truncated data in OPT and thus establish a more robust method must also be considered.

REFERENCES

[1] J. Sharpe, U. Ahlgren, P. Perry, B. Hill, A. Ross, J. Hecksher-Sorensen, R. Baldock, and D. Davidson, "Optical projection tomography as a tool for 3D microscopy and gene expression studies," *Science*, vol. 296, no. 5567, pp. 541–545, 2002.

[2] J. Sharpe, "Optical projection tomography," *Annu. Rev. Biomed. Eng.*, vol. 6, pp. 209–228, 2004.

[3] J. R. Walls, J. G. Sled, J. Sharpe, and R. M. Henkelman, "Resolution improvement in emission optical projection tomography," *Phys. Med. Biol.*, vol. 52, no. 10, pp. 2775–2790, 2007.

[4] F. Vasefi, E. Ng, B. Kaminska, G. H. Chapman, K. Jordan, and J. J. L. Carson, "Transmission and fluorescence angular domain optical projection tomography of turbid media," *Appl. Opt.*, vol. 48, no. 33, pp. 6448–6457, Nov. 2009.

[5] J. McGinty, K. B. Tahir, R. Laine, C. B. Talbot, C. Dunsby, M. A. Neil, L. Quintana, J. Swoger, J. Sharpe, and P. M. French, "Fluorescence lifetime optical projection tomography," *J. Biophoton.*, vol. 1, no. 5, pp. 390–394, 2008.

[6] C. Vinegoni, D. Razansky, J.-L. Figueiredo, M. Nahrendorf, V. Ntziachristos, and R. Weissleder, "Normalized born ratio for fluorescence optical projection tomography," *Opt. Lett.*, vol. 34, no. 3, pp. 319–321, Feb. 2009.

[7] R.-a. Lorbeer, M. Heidrich, C. Lorbeer, D. Fernando, R. Ojeda, G. Bicker, H. Meyer, and A. Heisterkamp, "Highly efficient 3D fluorescence microscopy with a scanning laser optical tomograph," *Opt. Express*, vol. 19, no. 6, pp. 412–417, 2011.

[8] J. Ripoll, H. Meyer, and A. Garofalakis, "*In vivo* optical tomography: From diffusion to ballistic," *Opt. Mater.*, vol. 31, no. 7, pp. 1082–1085, 2009.

[9] R. J. Bryson-Richardson and P. D. Currie, "Optical projection tomography for spatio-temporal analysis in the zebrafish," *Method. Cell Biol.*, vol. 76, pp. 37–50, Jan. 2004.

[10] J.-F. Colas and J. Sharpe, "Live optical projection tomography," *Organogenesis*, vol. 5, no. 4, pp. 211–216, Oct. 2009.

[11] J. Kerwin, M. Scott, J. Sharpe, L. Puelles, S. C. Robson, M. Martínez-de-la Torre, J. L. Ferran, G. Feng, R. Baldock, T. Strachan, D. Davidson, and S. Lindsay, "3 dimensional modelling of early human brain development using optical projection tomography," *BMC Neurosci.*, vol. 5, p. 27, 2004. Available: http://dx.doi.org/10.1186/1471-2202-5-27

[12] M. Rieckher, U. J. Birk, H. Meyer, J. Ripoll, and N. Tavernarakis, "Microscopic optical projection tomography *In Vivo*," *PLoS ONE*, vol. 6, no. 4, p. e18963, Apr. 2011. Available: http://dx.doi.org/10.1186/1471-2202-5-27.

[13] H. Meyer, A. Darrell, A. Metaxakis, C. Savakis, and J. Ripoll, "Optical projection tomography for in-vivo imaging of drosophila melanogaster," *Microsc. Anal.*, vol. 22, pp. 19–22, 2008.

[14] J. R. Walls, J. G. Sled, J. Sharpe, and R. M. Henkelman, "Correction of artefacts in optical projection tomography," *Phys. Med. Biol.*, vol. 50, no. 19, pp. 4645–4665, 2005.

[15] P. F. Feruglio, C. Vinegoni, J. Gros, A. Sbarbati, and R. Weissleder, "Block matching 3D random noise filtering for absorption optical projection tomography," *Phys. Med. Biol.*, vol. 55, no. 18, pp. 5401–15, Sep. 2010.

[16] A. Darrell, H. Meyer, K. Marias, M. Brady, and J. Ripoll, "Weighted filtered backprojection for quantitative fluorescence optical projection tomography," *Phys. Med. Biol.*, vol. 53, no. 14, pp. 3863–3881, Jul. 2008.

[17] E. Betzig, G. H. Patterson, R. Sougrat, O. W. Lindwasser, S. Olenych, J. S. Bonifacino, M. W. Davidson, J. Lippincott-Schwartz, and H. F. Hess, "Imaging intracellular fluorescent proteins at nanometer resolution," *Science*, vol. 313, no. 5793, pp. 1642–1645, 2006.

[18] U. J. Birk, M. Rieckher, N. Konstantinides, A. Darrell, A. Sarasa-Renedo, H. Meyer, N. Tavernarakis, and J. Ripoll, "Correction for specimen movement and rotation errors for in-vivo optical projection tomography," *Biomed. Opt. Express*, vol. 1, no. 1, pp. 87–96, Aug. 2010.

[19] A. Cheddad, C. Svensson, J. Sharpe, F. Georgsson, and U. Ahlgren, "Image processing assisted algorithms for optical projection tomography," *IEEE Trans. Med. Imag.*, vol. 31, no. 1, pp. 1–15, Jan. 2012.

[20] S. Zhu, D. Dong, U. Birk, M. Rieckher, N. Tavernarakis, X. Qu, J. Liang, J. Tian, and J. Ripoll, "Automated motion correction for in vivo optical projection tomography," *IEEE Trans. Med. Imag.*, vol. 31, no. 7, pp. 1358–1371, Jul. 2012.

[21] S. Azevedo, D. Schneberk, J. Fitch, and H. Martz, "Calculation of the rotational centers in computed tomography sinograms," *IEEE Trans. Nucl. Sci.*, vol. 37, no. 4, pp. 1525–1540, Aug. 1990.

[22] Y. Wang and R. Wang, "Imaging using parallel integrals in optical projection tomography," *Phys. Med. Biol.*, vol. 51, no. 23, pp. 6023–6032, 2006.

[23] Y. Wang and R. K. Wang, "Optimization of image-forming optics for transmission optical projection tomography," *Appl. Opt.*, vol. 46, no. 27, pp. 6815–6820, Sep. 2007.

[24] S. Basu and Y. Bresler, "$O(N^3 \log N)$ backprojection algorithm for the 3D Radon transform," *IEEE Trans. Med. Imag.*, vol. 21, no. 2, pp. 76–88, Feb. 2002.

[25] C. Vinegoni, L. Fexon, P. F. Feruglio, M. Pivovarov, J.-L. Figueiredo, M. Nahrendorf, A. Pozzo, A. Sbarbati, and R. Weissleder, "High throughput transmission optical projection tomography using low cost graphics processing unit," *Opt. Express*, vol. 17, no. 25, pp. 22 320–22 332, Dec. 2009.

[26] D. Dong, J. Tian, Y. Dai, G. Yan, F. Yang, and P. wu, "Unified reconstruction framework for multi-modal medical imaging," *J. X-Ray Sci. Technol.*, vol. 19, pp. 111–126, 2011.

[27] U. J. Birk, A. Darrell, N. Konstantinides, A. Sarasa-Renedo, and J. Ripoll, "Improved reconstructions and generalized filtered back projection for optical projection tomography," *Appl. Opt.*, vol. 50, no. 4, pp. 392–398, Feb. 2011.

[28] M. Koukidou, A. Klinakis, C. Reboulakis, L. Zagoraiou, N. Tavernarakis, I. Livadaras, A. Economopoulos, and C. Savakis, "Germ line transformation of the olive fly bactrocera oleae using a versatile transgenesis marker," *Insect Mol. Biol.*, vol. 15, no. 1, pp. 95–103, 2006.

[29] M. Slaney and A. Kak, *Principles of Computerized Tomographic Imaging*. Philadelphia, PA: SIAM, 1988.

[30] S. Bainbridge and M. Bownes, "Staging the metamorphosis of drosophila melanogaster," *J. Embryol. Exp. Morphol.*, vol. 66, no. 1, pp. 57–80, 1981.

[31] V. Kumar, E. Scandella, R. Danuser, L. Onder, M. Nitschk, Y. Fukui, C. Halin, B. Ludewig, and J. V. Stein, "Global lymphoid tissue remodeling during a viral infection is orchestrated by a B cellClymphotoxin-dependent pathway," *Blood*, vol. 115, no. 23, pp. 4725–4733, 2010.

[32] Y. Kyriakou, R. M. Lapp, L. Hillebrand, D. Ertel, and W. A. Kalender, "Simultaneous misalignment correction for approximate circular cone-beam computed tomography," *Phys. Med. Biol.*, vol. 53, no. 22, pp. 6267–6289, 2008.

[33] A. Kingston, A. Sakellariou, T. Varslot, G. Myers, and A. Sheppard, "Reliable automatic alignment of tomographic projection data by passive auto-focus," *Med. Phys.*, vol. 38, no. 9, pp. 4934–4945, 2011.

Authors' photographs and biographies not available at the time of publication.